# Anisotropic electrodynamics of type-II Weyl semimetal candidate WTe_{2}

A. J. Frenzel, C. C. Homes, Q. D. Gibson, Y. M. Shao, K. W. Post, A. Charnukha, R. J. Cava, and D. N. Basov

# Anisotropic electrodynamics of type-II Weyl semimetal candidate WTe$_2$

A. J. Frenzel,[1] C. C. Homes,[2] Q. D. Gibson,[3] Y. M. Shao,[1,4]
K. W. Post,[1] A. Charnukha,[1] R. J. Cava,[3] and D. N. Basov[1,4]

[1]*Department of Physics, University of California, San Diego, La Jolla, CA 92039, USA*
[2]*Condensed Matter Physics and Materials Science Department,*
*Brookhaven National Laboratory, Upton, New York 11973, USA*
[3]*Department of Chemistry, Princeton University, Princeton, New Jersey 08544, USA*
[4]*Department of Physics, Columbia University, New York, NY 10027, USA*
(Dated: May 31, 2017)

We investigated the *ab*-plane optical properties of single crystals of WTe$_2$ for light polarized parallel and perpendicular to the W-chain axis over a broad range of frequency and temperature. At far-infrared frequencies, we observed a striking dependence of the reflectance edge on light polarization, corresponding to anisotropy of the carrier effective masses. We quantitatively studied the temperature dependence of the plasma frequency, revealing a modest increase of the effective mass anisotropy in the *ab*-plane upon cooling. We also found strongly anisotropic interband transitions persisting to high photon energies. These results were analyzed by comparison with *ab initio* calculations. The calculated and measured plasma frequencies agree to within 10% for both polarizations, while the calculated interband conductivity shows excellent agreement with experiment.

Tungsten ditelluride (WTe$_2$) is a semimetallic transition metal dichalcogenide which exhibits extreme magnetoresistance resulting from the nearly-perfect compensation between electron and hole populations, along with its extraordinarily high mobility.[1–7] Recent theoretical predictions[8] and experimental measurements[9–13] suggest that it may be a type-II Weyl semimetal with tilted Weyl cones residing above the Fermi energy, though the topology is not yet firmly established[14]. Its orthorhombic crystal structure comprises planes of distorted triangular lattices of tungsten atoms sandwiched by tellurium atoms. The distortion of the triangular lattices generates quasi-one-dimensional chains of tungsten atoms, leading to strongly anisotropic electronic properties.[15–17] Optical measurements provide a powerful tool to investigate electronic structure which complements photoemission and tunneling measurements due to its sensitivity to the role of electronic interactions in solids.[18–20] In a previous optical study,[21] only the average in-plane electrodynamic response was measured, resulting in limited access to the underlying electronic structure. Here, we report anisotropic electrodynamics in WTe$_2$ observed by measuring the reflection of polarized light from single crystal samples.

Single crystals of WTe$_2$ were synthesized using the flux growth method.[3] We performed near-normal incidence reflectance measurements using Fourier transform infrared spectroscopy for light frequencies 100 - 8000 cm$^{-1}$, which we supplemented with variable-angle spectroscopic ellipsometry for frequencies 6000 - 25000 cm$^{-1}$. Ellipsometric data were obtained and analyzed using protocols appropriate for orthorhombic crystals.[22] Optical constants were extracted from the reflectance data by a Kramers-Kronig transformation, with Hagen-Rubens form for the low-frequency extrapolation. At high frequencies, the reflectance was extrapolated as a constant to 85000 cm$^{-1}$ then decayed as $\omega^{-4}$ to 2.5×10$^6$ cm$^{-1}$ (Ref. 23). This extrapolation ensured that the optical constants obtained from the Kramers-Kronig transformation agreed with those retrieved directly from the ellipsometric data in the overlap region.

Figure 1 displays the reflectance of WTe$_2$ in the infrared spectral range for the two polarizations. The smooth, featureless room temperature spectra develop a sharp edge as the temperature is lowered. The minimum in reflectance occurs near the screened plasma frequency $\omega_p^* = \omega_p/\sqrt{\epsilon_\infty^*}$, where $\omega_p^2 = 4\pi ne^2/m^*$ and $\epsilon_\infty^*$ is the contribution to the dielectric function due to interband optical transitions.[24] Here $m^*$ is the effective mass, $n$ is the carrier density, and $e$ is the electron charge. At 10 K, this reflectance edge occurs at approximately 600 cm$^{-1}$ for incident radiation polarized along the crystallographic *a*-axis (along the W chains;[2] top panel), while for light polarized along the *b*-axis, the reflectance edge occurs around 440 cm$^{-1}$ (bottom panel), yielding an anisotropy ratio $\omega_{p,a}^*/\omega_{p,b}^* \sim 1.3$. This anisotropy may reflect differences in both the effective masses and $\epsilon_\infty^*$. Therefore, in order to determine the mass anisotropy, the dielectric function must be fit directly.

The dielectric functions calculated from a Kramers-Kronig analysis of the 10 K reflectance in Fig. 1 are plotted in Fig. 2, exhibiting the expected zero crossings at the screened plasma frequencies $\omega_{p,a}^* \approx 600$ cm$^{-1}$ and $\omega_{p,b}^* \approx 440$ cm$^{-1}$. Density functional theory calculations,[2,14,21,25,26] ARPES,[5,27,28] and quantum oscillations measurements[6,29–32] all reveal that WTe$_2$ possesses at least four distinct bands crossing the Fermi level on each side of the $\Gamma$ point of the Brillouin zone (two electron pockets and two hole pockets along the $\Gamma-X$ high symmetry direction; see Fig. 5a). Therefore, following a previous report,[21] we fit our low-temperature data with two Drude components, which we interpret as corresponding to electron carriers and hole carriers. The dielectric function used to model the data shown in Fig.
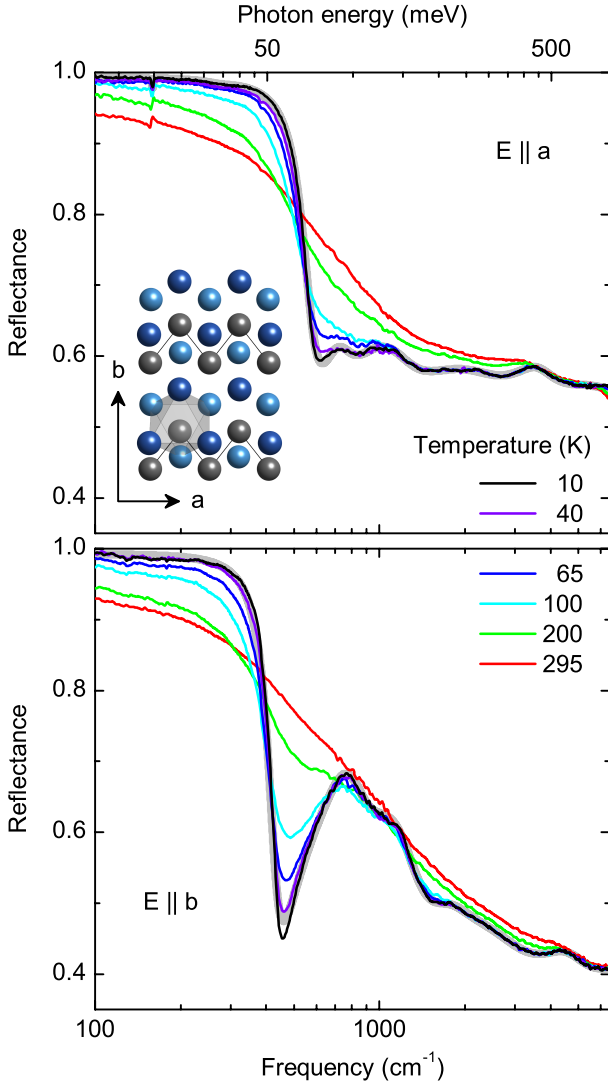
FIG. 1. (color) Reflectance of WTe$_2$ measured for light polarized parallel to the crystallographic $a$-axis (top panel) and $b$-axis (bottom panel). At low temperatures, the reflectance along both directions develops a pronounced plasma edge, with the frequency differing strongly for the two axes. Reflectance curves calculated from Drude-Lorentz fits to the 10 K dielectric function (see text) are plotted as thick gray lines. Inset of the top panel shows a single layer of the WTe$_2$ crystal structure viewed along the $c$-axis. Grey represents W atoms, dark blue represents Te atoms in the top layer of the sandwich, and light blue represents Te atoms in the bottom layer of the sandwich. A single distorted Te octahedron is shown, as well as the bonds between nearest W atoms, highlighting the anisotropic chain structure along the $a$-axis.

2 is given by[21]

$$\epsilon(\omega) = \epsilon_\infty - \sum_{j=1}^{2} \frac{\omega_{p,j}^2}{\omega^2 + i\omega/\tau_j} + \sum_k \frac{\Omega_{p,k}^2}{\omega_{0,k}^2 - \omega^2 - i\omega\gamma_k}. \quad (1)$$

Here $\omega_{p,j}$ are the free carrier plasma frequencies, $\tau_j$ are the free carrier scattering times, $\Omega_{p,k}$ are the oscillator
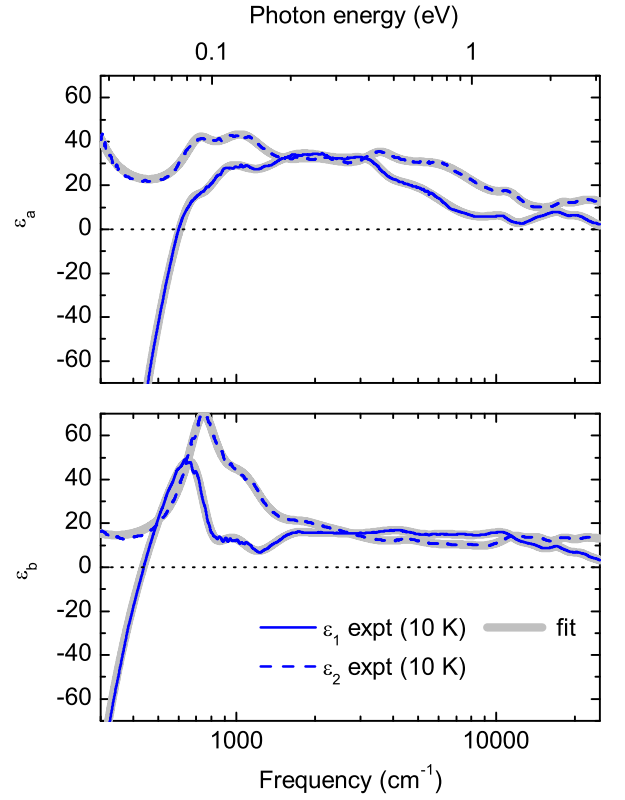


FIG. 2. (color) Dielectric function extracted from Kramers-Kronig analysis of the reflectance data shown in Fig. 1 for the crystallographic $a$-axis (top panel, blue lines) and $b$-axis (bottom panel, blue lines), along with fits to Eq. 1 (grey lines). The spectra are characterized by zero crossings at the screened plasma frequencies, 580 $^{-1}$ cm$^{-1}$ for the $a$-axis and 440 cm$^{-1}$ for the $b$-axis.

strengths for phonons and/or interband electronic transitions, $\omega_{0,k}$ are the phonon and/or interband transition energies, and $\gamma_k$ are the half-widths of these transitions.

The bare plasma frequencies extracted from fits to Eq. (1) as $\omega_{p,a}^2 = \omega_{p,a,1}^2 + \omega_{p,a,2}^2$ and $\omega_{p,b}^2 = \omega_{p,b,1}^2 + \omega_{p,b,2}^2$ are displayed in the top panel of Fig. 3. The plasma frequencies only weakly depend on temperature as compared to more familiar semimetals such as bismuth[33] and graphite.[34] The anisotropy ratio $\omega_{p,a}/\omega_{p,b}$ approaches $\sim$1.5 at low temperature. Since the square of the plasma frequency is inversely proportional to the effective mass, $\omega_p^2 \propto 1/m^*$, these values provide access to the effective mass anisotropy for the two crystal axes. The extracted mass anisotropy ratio $\eta_{ab} = m_b^*/m_a^* = \omega_{p,a}^2/\omega_{p,b}^2 \sim 2.2$ we observed changes by $\approx$35% upon cooling from room temperature to 10 K (lower panel of Fig. 3). This may reflect the sensitivity of the band structure to changes in lattice constants,[13] shift of the chemical potential with temperature,[5,27] or thermal population of bands nearby in energy with different effective masses.[35] Additionally, $\eta_{ab}$ is approximately constant below 100K. We did not detect significant anisotropy in the fitted scattering rates,
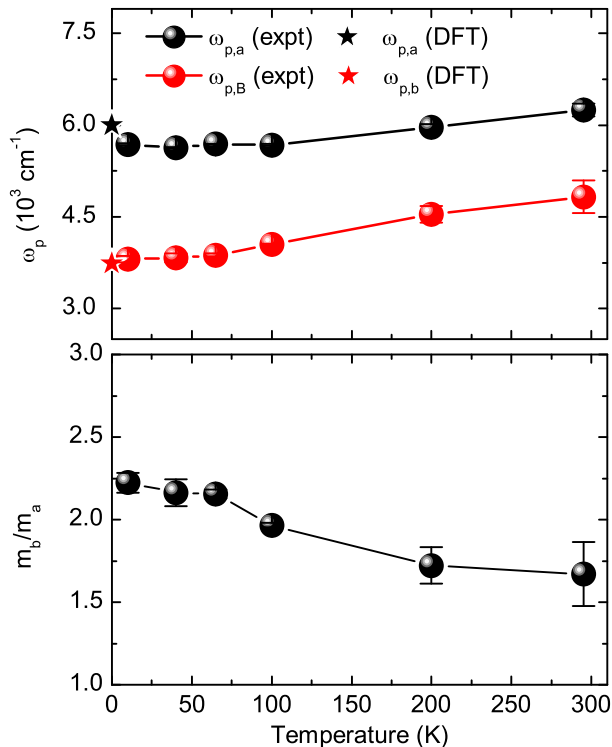
FIG. 3. (color) Top panel: Bare plasma frequencies for $a$- and $b$-axis polarized light at various temperatures extracted by fitting the dielectric functions to Eq. (1) (spheres), compared to the value calculated from first principles (stars). Bottom panel: Ratio of effective mass for $b$-axis to effective mass for $a$-axis as a function of temperature, showing a smooth increase of $\approx 35\%$ upon cooling from room temperature to 10 K.

which agree well with the values reported previously.[21]

The mass anisotropy and modest temperature dependence we detected contrasts sharply with the strong temperature dependence observed in the $ac$ mass anisotropy extracted from the angle-resolved magnetoresistance measurements of Ref. 36. In that work, the out-of-plane mass anisotropy $\eta_{ac}$ was inferred to be near 2 at high temperatures and to approach 5 at low temperatures, with a sharp turn-on around 50 K. The difference in magnitude of the anisotropy for in-plane masses versus out-of-plane masses is expected from the crystal structure of $WTe_2$. While the $ab$-plane is composed of a distorted triangular lattice with quasi-1D chains, the covalent bonds along the $b$-axis (perpendicular to the chains) are still stronger than the inter-plane van der Waals bonds along the $c$-axis.[17] This is also reflected in the Fermi surface extracted from first principles calculations and quantum oscillations, as discussed below. The stronger temperature dependence of $\eta_{ac}$ may reflect the fact that the $c$-axis lattice constant depends more sensitively on temperature than the in-plane lattice constants.[13] Additionally, the different dispersion along distinct axes influences how changes to the chemical potential alter the effective masses, leading to the different temperature dependence observed for $\eta_{ab}$

TABLE I. Fitted parameters compared to those obtained from density functional theory.

|  | Experiment (10 K) | Density functional theory |
| --- | --- | --- |
| $\omega_{p,a}$ (cm$^{-1}$) | $5683 \pm 16$ | 6000 |
| $\epsilon^*_{\infty,a}$ | $91.0 \pm 0.9$ | 60 |
| $\omega_{p,b}$ (cm$^{-1}$) | $3810 \pm 50$ | 3730 |
| $\epsilon^*_{\infty,b}$ | $74.7 \pm 1.5$ | 52 |
| $\eta_{ab}$ | $2.22 \pm 0.06$ | 2.59 |

and $\eta_{ac}$.

We compared the measured plasma frequencies to those calculated from density functional theory and measured by quantum oscillations.[30] Our density functional theory-based calculations were performed using the generalized gradient approximation, including spin-orbit interaction[37,38] (GGA+SOC, this work; see supplementary material of Ref. 21 for details of the calculations), yielding $\omega_{p,a} \approx 6000$ cm$^{-1}$ and $\omega_{p,b} \approx 3700$ cm$^{-1}$, reproducing the experimental results well (Table I). This close match between calculated and measured plasma frequency indicates that electronic correlations do not strongly influence the electrodynamics in $WTe_2$.[18,19] To compare to quantum oscillations, we used $k_F$ reported in Ref. 30 and in-plane cyclotron masses from the supplementary material of Ref. 27. We further approximated the dispersion as parabolic to obtain plasma frequencies $\omega_{p,a} \approx 5800$ cm$^{-1}$ and $\omega_{p,b} \approx 4000$ cm$^{-1}$, in good agreement with our low-temperature measurements. We note that these results from quantum oscillations are consistent with our measured $\eta_{ab} \sim 2$, as well as $\eta_{ac} \sim 5$ reported in Ref. 36.

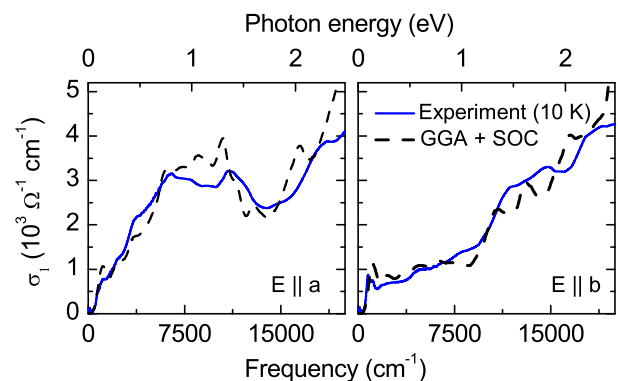We also extracted the optical conductivity from our



FIG. 4. (color) Interband optical conductivity of $WTe_2$ measured along the crystallographic $a$-axis (blue line; left panel) and $b$-axis (blue line; right panel), along with corresponding theoretical calculation of the optical conductivity from density functional theory (black dashed lines; both panels). The calculated conductivity captures the main features of the experimental data over a broad range of photon energy.
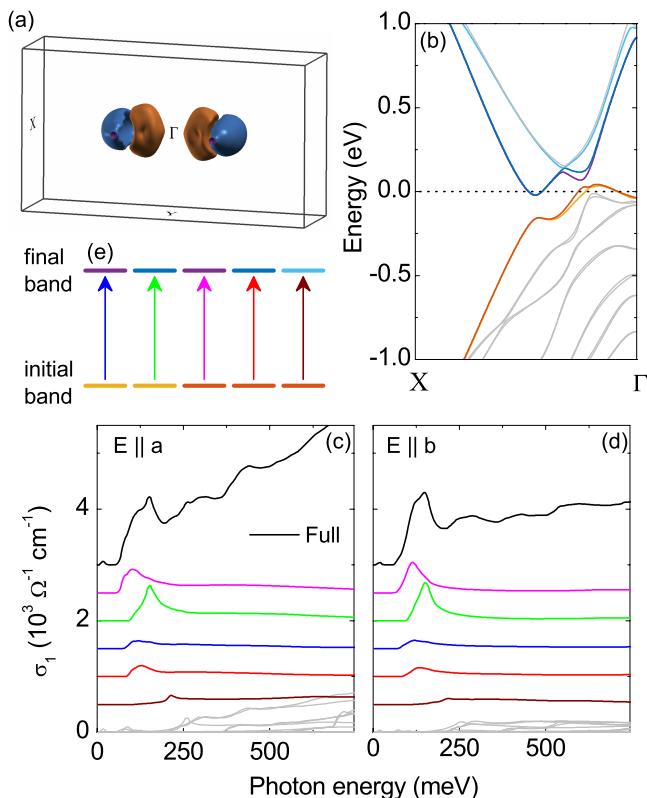
FIG. 5. (color) First-principles calculations of interband optical conductivity. (a) The Fermi surface in the first Brillouin zone, showing electron pockets in blue and hole pockets in orange (generated using XCrysDen[39]). (b) Band dispersion along the $\Gamma-X$ direction, with the five bands which contribute most strongly to low-energy interband transitions colored. (c-d) Decomposition of interband conductivity into individual band-to-band transitions for light polarized along the $a$-axis (c) and $b$-axis (d). The five strongest low-energy transitions are colored to match with the transitions shown in the simplified energy diagram of panel (e) and offset by 500 $\Omega^{-1}$ cm$^{-1}$ for clarity.

data as $\sigma(\omega) = -2\pi i\omega[\epsilon(\omega) - \epsilon_\infty]/Z_0$, with $Z_0 \approx 377$ $\Omega$ the impedance of free space, to compare with first-principles calculations.[38] The experimental data with Drude contribution subtracted are shown in Fig. 4 (blue lines), revealing a sizeable anisotropy in the strength of interband transitions for the two axes. Below 12000 cm$^{-1}$, the absorption is stronger along the $a$-axis, but the $b$-axis conductivity dominates above this frequency until they finally merge at $\sim$20000 cm$^{-1}$. We plot the results of our $ab$ $initio$ calculations as black dashed lines in Fig. 4. Remarkably, the experimental conductivity is extremely well-reproduced by the calculation.

As noted in Ref. 21, the interband conductivity appears to grow approximately linearly with frequency. Our polarized measurements reveal that this behavior is especially pronounced along the $a$-axis. This is the expected behavior for Dirac and Weyl semimetals.[40–48] The calculations presented in Refs. 8 and 13, however, reveal that

the Weyl points in WTe$_2$ lie well above the Fermi level. Optical measurements probe transitions from filled states to empty states, so our measurements are not sensitive to transitions between Weyl cones. Instead, they are only sensitive to transitions from topologically trivial occupied bands to both topologically trivial and nontrivial unoccupied bands. Additionally, the energy separation for direct transitions between upper and lower Weyl cones is expected to be $\sim$5 - 10 meV (40 - 80 cm$^{-1}$),[8,13] which overlaps with the free carrier response and is below our experimental low-frequency cutoff. This energy separation also implies that transitions from trivial to nontrivial bands would lie within a narrow frequency range, making a negligible contribution to the measured conductivity. It is thus likely that the observed interband conductivity can be fully accounted for by transitions between topologically trivial bands.

To elucidate the origin of the measured optical response, we have decomposed the interband conductivity into contributions from different bands near the Fermi level. The results of the calculations are presented in Figs. 5c-d. In these panels, the five strongest low-energy interband transitions are colored and offset by 500 $\Omega^{-1}$ cm$^{-1}$ for clarity, with the full interband conductivity shown as black lines. For the remaining contributions to the interband transitions, each thin grey line represents the sum over all transitions originating from the same initial band. The relevant band dispersions along the $\Gamma-X$ direction are shown in panel (b), and the transitions are shown in a simplified energy diagram in panel (e). Here, the color of the initial and final energy levels corresponds to the bands in panel (b) and the arrow colors match the colors of the conductivity contributions in panels (c-d). These results demonstrate that the interband conductivity in WTe$_2$, including the approximately linear region, is comprised of dozens of trivial band-to-band transitions.

In conclusion, we reported measurements of the anisotropic electrodynamics of carriers in the semimetal WTe$_2$. We found an average mass anisotropy ratio of $\sim$2.2 for the $a$ and $b$ lattice directions, in agreement with quantum oscillations measurements and first principles calculations. This anisotropy ratio was found to exhibit moderate dependence on temperature. We also demonstrated that the interband conductivity can be understood as arising from numerous band-to-band transitions without invoking Weyl physics. These results serve as an important baseline to inform future optical measurements of other potential Weyl semimetals. In particular, our analysis reveals that caution must be exercised when ascribing linear frequency dependence of the optical conductivity to Weyl physics or to a superposition of many trivial interband transitions.

[1] A. B. Pippard, *Magnetoresistance in Metals* (Cambridge University Press, Cambridge, 1989).

[2] M. N. Ali, J. Xiong, S. Flynn, J. Tao, Q. D. Gibson, L. M. Schoop, T. Liang, N. Haldolaarachchige, M. Hirschberger, N. P. Ong, and R. J. Cava, Nature **514**, 205 (2014).

[3] M. N. Ali, L. Schoop, J. Xiong, S. Flynn, Q. Gibson, M. Hirschberger, N. P. Ong, and R. J. Cava, Europhys. Lett. **110**, 67002 (2015).

[4] H. Y. Lv, W. J. Lu, D. F. Shao, Y. Liu, S. G. Tan, and Y. P. Sun, Europhys. Lett. **110**, 37004 (2015).

[5] I. Pletikosić, M. N. Ali, A. V. Fedorov, R. J. Cava, and T. Valla, Phys. Rev. Lett. **113**, 216601 (2014).

[6] L. Wang, I. Gutiérrez-Lezama, C. Barreteau, N. Ubrig, E. Giannini, and A. F. Morpurgo, Nat. Commun. , 8892 (2015).

[7] V. Fatemi, Q. D. Gibson, K. Watanabe, T. Taniguchi, R. J. Cava, and P. Jarillo-Herrero, Phys. Rev. B **95**, 041410R (2017).

[8] A. A. Soluyanov, D. Gresch, Z. Wang, Q. Wu, M. Troyer, X. Dai, and B. A. Bernevig, Nature **527**, 495 (2015).

[9] Y. Wu, D. Mou, N. H. Jo, K. Sun, L. Huang, S. L. Bud'ko, P. C. Canfield, and A. Kaminski, Phys. Rev. B **94**, 121113 (2016).

[10] J. Sánchez-Barriga, M. G. Vergniory, D. Evtushinsky, I. Aguilera, A. Varykhalov, S. Blügel, and O. Rader, Phys. Rev. B **94**, 161401 (2016).

[11] C. Wang, Y. Zhang, J. Huang, S. Nie, G. Liu, A. Liang, Y. Zhang, B. Shen, J. Liu, C. Hu, Y. Ding, D. Liu, Y. Hu, S. He, L. Zhao, L. Yu, J. Hu, J. Wei, Z. Mao, Y. Shi, X. Jia, F. Zhang, S. Zhang, F. Yang, Z. Wang, Q. Peng, H. Weng, X. Dai, Z. Fang, Z. Xu, C. Chen, and X. J. Zhou, Phys. Rev. B **94**, 241119 (2016).

[12] Y. Wang, E. Liu, H. Liu, Y. Pan, L. Zhang, J. Zeng, Y. Fu, M. Wang, K. Xu, Z. Huang, Z. Wang, H. Lu, D. Xing, B. Wang, X. Wan, and F. Miao, Nat. Commun. **7**, 13142 (2016).

[13] Y.-Y. Lv, X. Li, B.-B. Zhang, W. Y. Deng, S.-H. Yao, Y. B. Chen, J. Zhou, S.-T. Zhang, M.-H. Lu, L. Zhang, M. Tian, L. Sheng, and Y.-F. Chen, Phys. Rev. Lett. **118**, 096603 (2017).

[14] F. Y. Bruno, A. Tamai, Q. S. Wu, I. Cucchi, C. Barreteau, A. de la Torre, S. McKeown Walker, S. Riccò, Z. Wang, T. K. Kim, M. Hoesch, M. Shi, N. C. Plumb, E. Giannini, A. A. Soluyanov, and F. Baumberger, Phys. Rev. B **94**, 121112 (2016).

[15] B. E. Brown, Acta Crystallogr. **20**, 268 (1966).

[16] W. G. Dawson and D. W. Bullett, J. Phys. C Solid State Phys. **20**, 6159 (1987).

[17] A. Mar, S. Jobic, and J. A. Ibers, J. Am. Chem. Soc. **114**, 8963 (1992).

[18] D. N. Basov, R. D. Averitt, D. van der Marel, M. Dressel, and K. Haule, Rev. Mod. Phys. **83**, 471 (2011).

[19] M. M. Qazilbash, J. J. Hamlin, R. E. Baumbach, L. Zhang, D. J. Singh, M. B. Maple, and D. N. Basov, Nat. Phys. **5**, 647 (2009).

[20] A. Charnukha, K. W. Post, S. Thirupathaiah, D. Pröpper, S. Wurmehl, M. Roslova, I. Morozov, B. Büchner, A. N. Yaresko, A. V. Boris, S. V. Borisenko, and D. N. Basov, Sci. Rep. **6**, 18620 (2016).

[21] C. C. Homes, M. N. Ali, and R. J. Cava, Phys. Rev. B **92**, 161109 (2015).

[22] D. E. Aspnes, J. Opt. Soc. Am. **70**, 1275 (1980).

[23] F. Wooten, *Optical Properties of Solids* (Academic Press, New York, 1972).

[24] N. P. Armitage, R. Tediosi, F. Lévy, E. Giannini, L. Forro, and D. van der Marel, Phys. Rev. Lett. **104**, 237401 (2010).

[25] J. Augustin, V. Eyert, T. Böker, W. Frentrup, H. Dwelk, C. Janowitz, and R. Manzke, Phys. Rev. B **62**, 10812 (2000).

[26] Q. Li, J. Yan, B. Yang, Y. Zang, J. Zhang, K. He, M. Wu, Y. Zhao, D. Mandrus, J. Wang, Q. Xue, L. Chi, D. J. Singh, and M. Pan, Phys. Rev. B **94**, 115419 (2016).

[27] Y. Wu, N. H. Jo, M. Ochi, L. Huang, D. Mou, S. L. Bud'ko, P. C. Canfield, N. Trivedi, R. Arita, and A. Kaminski, Phys. Rev. Lett. **115**, 166602 (2015).

[28] P. K. Das, D. Di Sante, I. Vobornik, J. Fujii, T. Okuda, E. Bruyer, A. Gyenis, B. E. Feldman, J. Tao, R. Ciancio, G. Rossi, M. N. Ali, S. Picozzi, A. Yadzani, G. Panaccione, and R. J. Cava, Nat. Commun. **7**, 10847 (2016).

[29] P. L. Cai, J. Hu, L. P. He, J. Pan, X. C. Hong, Z. Zhang, J. Zhang, J. Wei, Z. Q. Mao, and S. Y. Li, Phys. Rev. Lett. **115**, 057202 (2015).

[30] Z. Zhu, X. Lin, J. Liu, B. Fauqué, Q. Tao, C. Yang, Y. Shi, and K. Behnia, Phys. Rev. Lett. **114**, 176601 (2015).

[31] D. Rhodes, S. Das, Q. R. Zhang, B. Zeng, N. R. Pradhan, N. Kikugawa, E. Manousakis, and L. Balicas, Phys. Rev. B **92**, 125152 (2015).

[32] Y. Zhao, H. Liu, J. Yan, W. An, J. Liu, X. Zhang, H. Wang, Y. Liu, H. Jiang, Q. Li, Y. Wang, X.-Z. Li, D. Mandrus, X. C. Xie, M. Pan, and J. Wang, Phys. Rev. B **92**, 041104 (2015).

[33] R. Tediosi, N. P. Armitage, E. Giannini, and D. van der Marel, Phys. Rev. Lett. **99**, 016406 (2007).

[34] A. B. Kuzmenko, E. van Heumen, F. Carbone, and D. van der Marel, Phys. Rev. Lett. **100**, 117401 (2008).

[35] H. J. Park, L. J. Sandilands, J. S. You, H. S. Ji, C. H. Sohn, J. W. Han, S. J. Moon, K. W. Kim, J. H. Shim, J. S. Kim, and T. W. Noh, Phys. Rev. B **93**, 205122 (2016).

[36] L. R. Thoutam, Y. L. Wang, Z. L. Xiao, S. Das, A. Luican-Mayer, R. Divan, G. W. Crabtree, and W. K. Kwok, Phys. Rev. Lett. **115**, 046602 (2015).

[37] D. J. Singh, *Planewaves, Pseudopotentials and the LAPW Method* (Kluwer Academic, Boston, 1994).

[38] C. Ambrosch-Draxl and J. O. Sofo, Comput. Phys. Commun. **175**, 1 (2006).

[39] A. Kokalj, Comput. Mater. Sci. **28**, 155 (2003).

[40] T. Timusk, J. P. Carbotte, C. C. Homes, D. N. Basov, and S. G. Sharapov, Phys. Rev. B **87**, 235121 (2013).

[41] P. E. C. Ashby and J. P. Carbotte, Phys. Rev. B **89**, 245121 (2014).

[42] R. Y. Chen, Z. G. Chen, X.-Y. Song, J. A. Schneeloch, G. D. Gu, F. Wang, and N. L. Wang, Phys. Rev. Lett. **115**, 176404 (2015).

[43] A. B. Sushkov, J. B. Hofmann, G. S. Jenkins, J. Ishikawa, S. Nakatsuji, S. Das Sarma, and H. D. Drew, Phys. Rev. B **92**, 241108 (2015).

[44] D. Neubauer, J. P. Carbotte, A. A. Nateprov, A. Löhle, M. Dressel, and A. V. Pronin, Phys. Rev. B **93**, 121202 (2016).

[45] B. Xu, Y. M. Dai, L. X. Zhao, K. Wang, R. Yang, W. Zhang, J. Y. Liu, H. Xiao, G. F. Chen, A. J. Taylor, D. A. Yarotski, R. P. Prasankumar, and X. G. Qiu, Phys. Rev. B **93**, 121110 (2016).

[46] A. Akrap, M. Hakl, S. Tchoumakov, I. Crassee, J. Kuba, M. O. Goerbig, C. C. Homes, O. Caha, J. Novák, F. Teppe, W. Desrat, S. Koohpayeh, L. Wu, N. P. Armitage, A. Nateprov, E. Arushanov, Q. D. Gibson, R. J. Cava, D. van der Marel, B. A. Piot, C. Faugeras, G. Martinez, M. Potemski, and M. Orlita, Phys. Rev. Lett. **117**, 136401 (2016).

[47] C. J. Tabert, J. P. Carbotte, and E. J. Nicol, Phys. Rev. B **93**, 085426 (2016).

[48] J. P. Carbotte, Phys. Rev. B **94**, 165111 (2016).